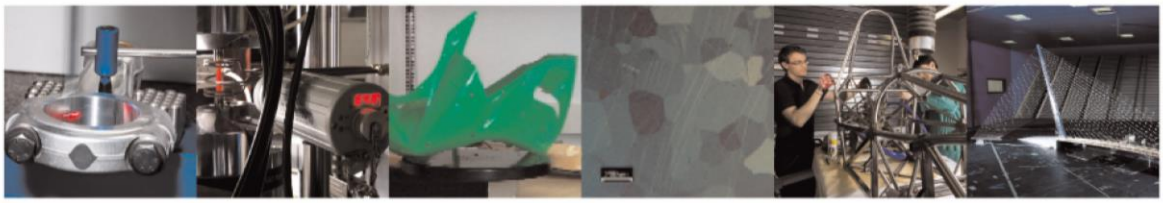

Investigation and characterization of an Al-Mg-Zr-Sc alloy with reduced Sc content for laser powder bed fusion

F. Belelli, R. Casati, C. Andrianopoli, F. Cuccaro, M. Vedani

This is a post-peer-review, pre-copyedit version of an article published in journal title. The final authenticated version is available online at: https://doi.org/10.1016/j.jallcom.2022.166519

DIPARTIMENTO DI MECCANICA ■ POLITECNICO DI MILANO
via G. La Masa, 1 ■ 20156 Milano ■ EMAIL (PEC): pecmecc@cert.polimi.it
http://www.mecc.polimi.it
Rev. 0

Investigation and characterization of an Al-Mg-Zr-Sc alloy with reduced Sc content for laser powder bed fusion

F. Belelli [a], R. Casati [a], C. Andrianopoli [b], F. Cuccaro [a], M. Vedani [a]

[a] Department of Mechanical Engineering, Politecnico di Milano, Via G. La Masa 1, 20156 Milano, Italy

[b] m4p material solutions Italy srl - Corso F., Ferrucci 112, 10138 Torino, Italy

Abstract

Only few high strength Al alloys are processable by Laser Powder Bed Fusion due to the occurrence of hot cracks during solidification. In recent years, the addition of Zr and Sc in Al-Mg alloys revealed an effective solutions to suppress solidification cracking and improve strength. Nevertheless, since Sc is classified as a critical raw material by European Commission due to its high cost and supply risk, its content should be desiderably reduced. It is therefore necessary to focus on novel Al alloys featuring both enhanced processability and low amount of Sc. In this study, we investigated the microstructure and mechanical behavior of an Al-5.2Mg-0.8Zr-0.3Sc alloy, commercially available as m4p™ StrengthAl, produced by Laser Powder Bed Fusion. Simulations of equilibrium phase diagrams and Scheil solidification curves showed the precipitation of primary Al3Zr and Al3(Sc,Zr) in the liquid phase on cooling. These particles revealed able to act as nuclei for heterogeneous nucleation of grains, giving rise to a fine equiaxed structure which is able to suppress hot cracking and increase the processability of the Al-Mg-Zr-Sc alloy. Despite the reduced Sc content, the formation of secondary Al3(Sc,Zr) nano-phases during the annealing treatment led to a sharp increase of micro-hardness values, whereas a stress relief effect was monitored by residual stress measurements during aging. Both as-built and aged alloys show a bimodal grain size distribution and a similar crystallographic texture. Yield strength and ultimate tensile strength of 460 MPa and 485 MPa, respectively, were recorded in samples aged at 350 °C for 24 h and at 375 °C for 8 h.

Keywords

Metals and alloysLaser processingMicrostructurePrecipitation

1. Introduction

Additive Manufacturing (AM) technologies are widely used in several industrial sectors due to their ability to produce components with complex shapes and high performance-to-weight ratio. Among AM techniques for metals, Laser Powder Bed Fusion (LPBF) is the most widespread technology for prototyping and production of small series. In LPBF the material volume is built using a layer-by-layer strategy, in which a metallic powder bed is selectively melted by a high-energy laser beam. In each layer and along each distinct laser track, tiny melt pools are generated and their rapid solidification promotes the metallic bond with the underlying layers [1]. Despite the exponential growth of AM techniques, the availability of Al alloys suitable for LPBF processes is still limited [2]. Indeed, the majority of high-strength Al alloys suffers solidification cracking and feature a scarce LPBF processability [3], [4]. Specifically, local tensile stresses build-up due to the large thermal shrinkage experienced by the solidifying metal. During the final stages of solidification, when a liquid film still exists among grains, hot cracks can arise along grain boundaries depending on chemical composition of the alloy, extent of solidification temperature range and properties of the solidifying structure [5], [6]. Several models were developed during recent years to predict the phenomenon of solidification cracking. Rappaz et al. proposed a model in which nucleation of a cracks occurs when the pressure drop along the inter-dendritic space falls below a cavitation pressure value [7]. Despite the sound physical basis of this model, its high complexity led to the development of novel strategies able to easily identify the tendency of materials to crack during solidification. Kou proposed a simplified model and considered the value of the index $|dT/d(fs^{1/2})|$ near $fs \rightarrow 1$ as an indicator for crack susceptibility, where dT and fs are the solidification temperature range and the mass fraction of solid, respectively [8]. Since hot cracking is likely to occur during the final stages of solidification, i.e when a coherent solid network forms and liquid feeding of grain boundaries is hindered, a large solidification temperature range at this stage ($fs \rightarrow 1$) leads to long inter-dendritic channel, therefore to an higher tendency of the material to crack. To suppress this phenomenon, two methodologies were identified. The first one relies on the decrease of the solidification temperature range by adding alloying elements able to form an abundant eutectic phase mixture at the end of solidification [9], [10], [11]. The second strategy relies on the addition of nucleants capable to promote the heterogeneous nucleation of fine equiaxed grains instead of the expected coarse columnar grains. This microstructure suppresses the formation of long inter-dendritic channels, homogeneously distribute the low-melting segregates at grain boundaries and provide a more difficult path for crack propagation compared to columnar grains [12], [13], [14]. During the recent years, novel Al alloys processable by LPBF have been developed following these two strategies. 5xxx series Al alloys modified with Sc and Zr captured the attention of researchers due to their hot-crack resistance and remarkable mechanical properties. Zhou et al. investigated the LPBF processability of the AA5083 alloy with the addition of 0.7 wt% Zr. Zirconium promotes the formation of nano-scale L12-Al_3Zr inoculants, responsible for the heterogeneous nucleation of fine equiaxed grains and the suppression of hot cracks during solidification [15]. Scandium was also extensively used in

5xxx series Al alloys to enhance the nucleation potential of fine equiaxed grains. Specifically, Sc intervenes in the solidification sequence of the alloy with the formation of primary L12-Al3(Sc,Zr) crystal seeds in the liquid phase and precipitates as secondary Al3(Sc,Zr) phase during the aging treatment [16]. These particles are responsible for precipitation strengthening and pinning of grain boundaries, thus higher mechanical performances and enhanced microstructural stability of the alloy are achieved [17]. In refs. [18], [19], [20], several Al-Mg and Al-Zn-Mg alloys with addition of different Sc/Zr ratio were processed by LPBF and a refined microstructure with submicron-sized grains was observed. Specifically, a peculiar microstructure with a bimodal grain size distribution was found in the majority of published works [18], [19], [20], [21], [22]. A fine grain zone rich of Al3(Sc,Zr) precipitates is noticeable close to melt pool boundaries, whereas a zone with coarser elongated grains and free of Sc-rich particles was noticed in the center of the melt pools. These features are ascribed to different local temperature gradient and growth rates experienced by the melt in these distinct zones. [19]. Thermal treatment does not affect the bimodal grain structure, whereas it promotes the precipitation of further secondary Al3(Sc,Zr) particles homogeneously distributed in the α-Al matrix, as reported by Kuo and colleagues [23]. Remarkable mechanical properties were detected after the heat treatment, with tensile strength values up to 500 MPa for the Scalmalloy®, patented by APWORKS GmbH [24].

Even though the effect of Sc and Zr as grain refiner has been extensively studied in the literature, few studies were carried out on the influence of Zr/Sc ratio on the microstructure and precipitation behavior of Al alloys. Li and co-workers investigated an Al-7.0Zn-2.5Mg-0.2Cu-0.6(Sc-Zr) alloy produced by casting with different Zr/Sc ratios. The grain refinement effect of Zr is sharply enhanced by the addition of Sc in the chemical composition of the alloy, indicating the high efficiency of this alloying element as grain refiner [25]. Indeed, the majority of Al-Mg-Sc-Zr alloys specifically developed for LPBF features a higher content of Sc with respect to that of Zr [19], [20], [21], [22], [23], [24], [25]. Nevertheless, Sc has some issues related to its high cost and supply risk (at least for european companies), and it has been classified as a critical raw material by the European Commission [26]. Thus, the development of new Al alloys with lower Sc content is of paramount importance. The main goal of this work consists in investigating the behavior of a low-Sc Al-Mg-Zr-Sc (5xxx) alloy, called m4p™ StrengthAl, produced by LPBF. It is worth noting that this alloy contains less Sc than the more common Scalmalloy® (0.66 wt%) [19]. Particular attention was given to the combined effect of Zr and Sc on mechanisms of primary and secondary precipitation of the Al3(Sc,Zr) phase. Solidification curves and equilibrium phase diagrams were computed by Thermo-Calc software. Differential scanning calorimetry, simulations of precipitation reactions by PRISMA and aging tests were carried out to study secondary Al3(Sc,Zr) formation. Microstructural features of both as-built (AB) and aged alloys were investigated through optical, scanning electron microscopy and electron back-scattered diffraction (EBSD) analyses. The effect of the heat treatment schedules on the evolution of residual stresses, crystallographic texture and tensile properties was investigated.

2. Materials and methods

An Al-Mg-Zr-Sc powder, commercially available as m4p™ StrengthAl, was supplied by m4p material solutions GmbH. The chemical composition measured by EDS analysis and the geometrical characteristics of the powder are reported in Table 1. Three EDS measurements were performed on the feedstock powder and the standard deviation is< 0.1 wt% for each alloying element. Powder particles show a spherical morphology as it is visible from SEM image of Fig. 1.

Table 1. Chemical composition (in wt%) and powder particle size (D50 and Span) of the investigated Al-Mg-Zr-Sc powder.

	Mg	Si	Fe	Zr	Sc	Al	D50 [μm]	Span [(D90-D10)/D50]
Al-Mg-Zr-Sc	5.2	<0.1	0.1	0.8	0.3	Bal.	37.4	0.76

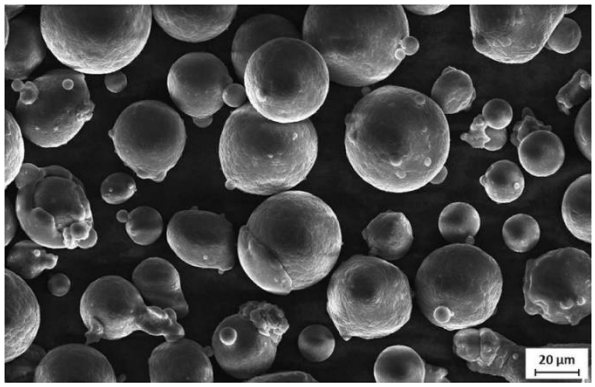

Fig. 1. SEM image of the as-received Al-Mg-Zr-Sc powder.

A Renishaw AM 250 machine equipped with a Reduced Build Volume device was used to produce 13 cubic samples (10 mm × 10 mm x 10 mm). A full-factorial DOE approach was performed for the optimization of LPBF process parameters. Hatch distance and point distance were varied between 70 μm and 130 μm and 52 μm and 108 μm, whereas layer thickness, exposure time and laser power were set at 25 μm, 140 μs and 200 W, respectively. The relative density of samples was measured by image analysis. Specifically, three light optical microscope (LOM) images were taken for each vertical section (parallel to the building direction) of the samples with 2.5x image magnification and the relative density was computed through ImageJ software, as the ratio between pore area and total area of the image. A maximum relative density of 99.97% was achieved using hatch distance and point distance of 120 μm and 54 μm, respectively, corresponding to a volumetric energy density of 173 J/mm3. These optimal LPBF parameters were used to produce prismatic samples (7 mm × 9 mm x 55 mm) with longitudinal axis orthogonal to the building direction. The positioning of the samples on the building platform is shown in Fig. 2. Tensile specimens (gauge length of 15 mm and cross-section diameter of 3 mm) were machined starting from the prismatic bars, complying with the ASTM E8/E8M standard [27]. Tensile tests were performed using a MTS-Alliance RT/100 universal machine equipped with a resistance extensometer. The

crosshead speed was set at 1 mm/min and three samples were tested for each condition at room temperature.

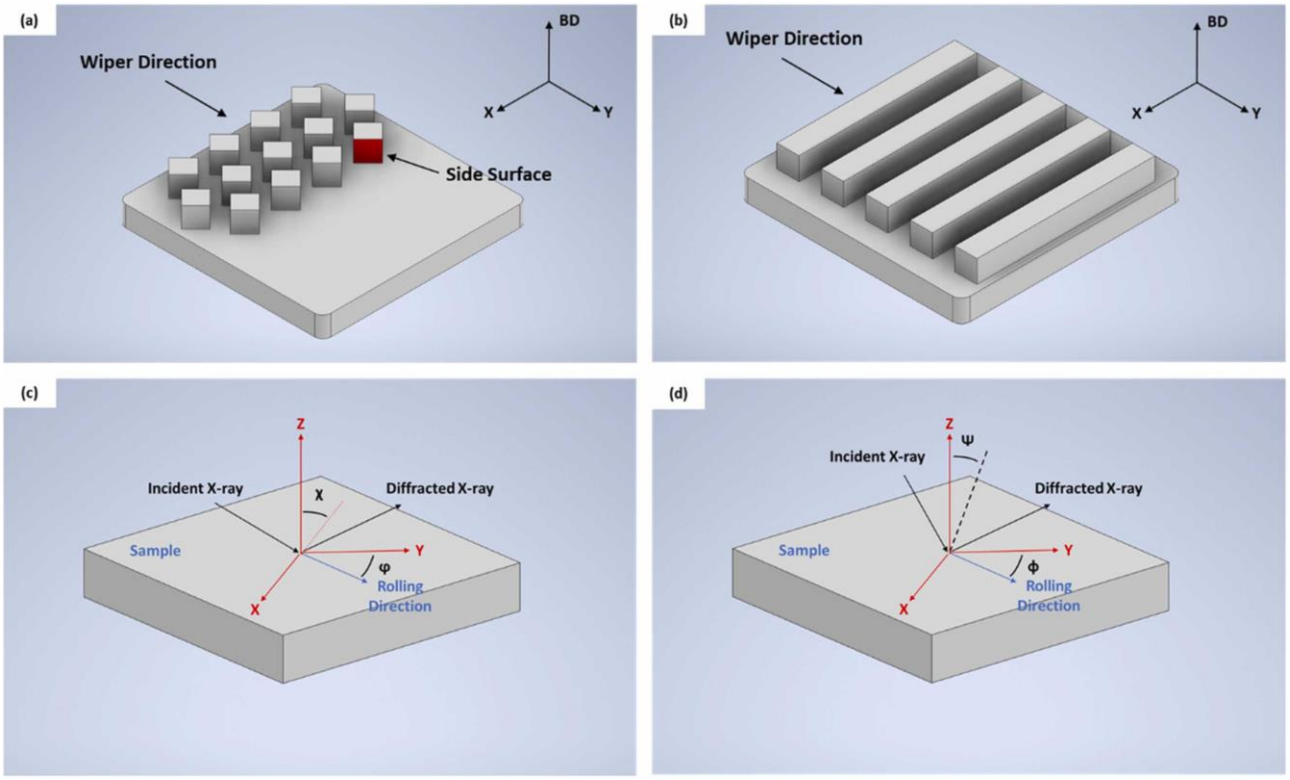

Fig. 2. A schematic of a) density samples and b) tensile specimens on the LPBF building platform. Representation of XRD reference system (axes highlighted in red) and sample orientation (rolling direction equals to the building direction of samples, depicted in blue) in c) texture and d) $\sin^2(\psi)$ stress measurement method.

A muffle furnace was used to perform aging treatments at temperatures ranging from 300 °C to 400 °C. The aging response of specimens for times ranging from 1 h to 24 h was monitored by Vickers micro-hardness tests performed with a load of 300 gF and a dwell time of 15 s. The micro-hardness measurements were carried out using a FM-810 Vickers tester produced by Tecmet2000. Five measurements were taken in the vertical section of samples and relatively far from the external surface, as described by the ASTM E92 – 17 standard [28].

Samples for metallographic analyses were grinded and polished using a Struers automatic machine and chemical etching was performed using Keller's reagent for 6 s. A Nikon Eclipse LV150NL light optical microscope (LOM) was used to collect images of sample sections for relative density analyses. A Zeiss Sigma 500 field emission scanning electron microscope (FE-SEM) equipped with Oxford Instruments Ultim Max detector for energy dispersive X-ray analysis (EDS) and electron backscatter diffraction (EBSD) detector mod. Oxford Instruments C-Nano was used for microstructure investigations. The software used to perform EBSD analyses and elaborate the data were Flamenco and Tango, developed by Oxford Instruments. Step size, critical misorientation angle and accelerating voltage were set at 0.15 µm, 10.0° and 20 kV, respectively, for all the analyses. X-ray diffraction (XRD) experiments were carried out with a Rigaku SmartLab SE multipurpose X-ray diffractometer equipped with copper

radiation source (Cuα1 of 1.54060 Å and Cuα2 of 1.54439 Å), D/teX Ultra 250 detector and Eulerian cradle with ϕ and χ rotation, operating at 40 kV and 40 mA. A scan rate of 1°/min and a step size of 0.02° was set for the diffraction patterns collected in Bragg-Brentano geometry. Texture measurements were performed on the vertical section of samples. Specimens were fixed onto the Eulerian cradle and rotated around ϕ (0–360°) and χ (15–90°) angles with a step size of 1° (see Fig. 2(c) for the definition of axes and angles). The intensity of three individual reflections of Al phase, namely (111), (200) and (220), was collected and Inverse Pole Figures (IPF) were computed for the investigated alloy in both as-built and aged conditions. The Eulerian cradle was also used to perform residual stress analyses on the side surface of printed specimens (highlighted in red in Fig. 1(a)). Measurements were carried out using the (311) reflection of Al phase as the reference peak. The sin2(ψ) method was exploited to compute residual stresses setting ψ values at 0°, − 9.97°, − 14.18°, − 17.46°, − 20.27°, − 22.79°, − 25.10°, − 27.27°, − 29.33°, − 31.31° and − 33.21° for each measurement. ψ is defined as the angle subtended by the bisector of the incident and diffracted beam and the normal to the sample surface, as depicted in Fig. 1(d). Due to the low penetration depth of X-rays, a plane stress condition was assumed to evaluate normal and shear residual stresses (σ11, σ22 and σ12, respectively) starting from the measured stress, according to the following equation [29]:

$$\sigma_{\varphi} = \sigma_{11} cos^2(\varphi) + \sigma_{12} \sin 2\varphi + \sigma_{22} sin^2(\varphi) \quad (1)$$

in which σϕ and ϕ are the measured stress value and the azimuth angle between the XRD reference system and the building direction of the sample, respectively (Fig. 1(c)). Performing the analysis along three different ϕ directions (0°, 45° and 90°), the Mohr's circle can be determined to evaluate the principal stresses (σI and σII) starting from the σ11, σ22 and σ12 values. The related standard deviations were calculated through error propagation methods.

Equilibrium phase diagrams, solidification curves and precipitation simulations of the investigated alloy were computed by ThermoCalc software (database TCAL 5: Al-Alloys v5.1). Scheil-Gulliver hypotheses were assumed for the simulation of the solidification curve [5]. TC-PRISMA module was used to simulate the precipitation kinetics of Al3(Sc,Zr) particles (database MOBAL 4: Al-Alloys Mobility v4.0). The nucleation, growth and coarsening of precipitates are modeled using the Langer-Schwartz theory [30].

3. Results

3.1. Simulations

The solidification curve of the Al-Mg-Zr-Sc alloy computed by Thermo-Calc software is shown in Fig. 3(a). The precipitation of the Al3Zr phase starts at 910 °C in the molten Al. Sc intervenes in the precipitation sequence with the formation of Al3(Sc,Zr) at 684 °C, followed by nucleation and growth of primary α-Al grains. Subsequently, Al13Fe4 and Mg2Si phases precipitate and α-Al-Al3Mg2 eutectic phase mixture forms during the last stages of

solidification. The fraction of Al3Zr and Al3(Sc,Zr) nuclei was computed as 1.48 wt% and 0.45 wt%, respectively (Fig. 3(b)).

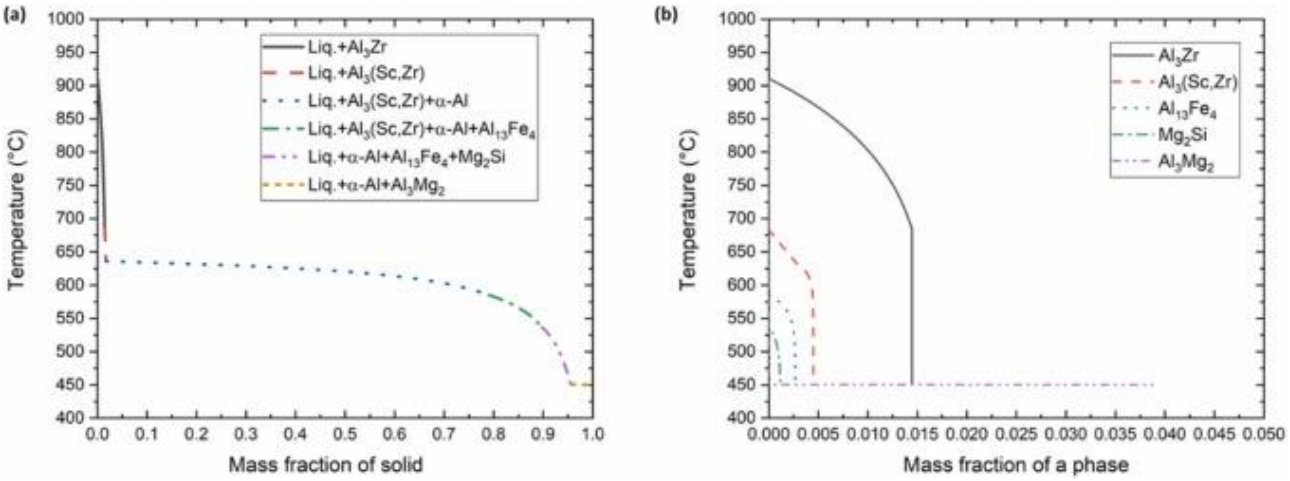

Fig. 3. a) Simulation of solidification curve of the Al-Mg-Zr-Sc alloy and b) mass fraction of second phases formed during solidification.

Simulations of the equilibrium phase diagram of Al-Zr and Al-Mg-Zr systems were performed to further investigate on the role of Zr on phase transformations. The most relevant results are reported in Fig. 4. Zr is responsible for a peritectic reaction at 660 °C in the Al-rich corner of the Al-Zr phase diagram. At temperatures higher than 660 °C, a mono-variant field with the coexistence of the liquid phase and the Al3Zr compound is noticeable for Zr content higher than 0.09 wt% (Fig. 4(a-b)). The addition of 4.5 wt% Mg is responsible for the decrease of the onset temperature of primary α-Al phase, and to the formation of the mono-variant Liquid+ α-Al field. Furthermore, the maximum solubility limit of Zr in α-Al decreases from 0.27 wt% to 0.05 wt% due to the high solubility of Mg atoms in the α-Al phase (Fig. 4(c-d)). Thus, a larger driving force is expected for the precipitation of Al3Zr phase during direct aging treatment in Al-Mg-Zr systems.

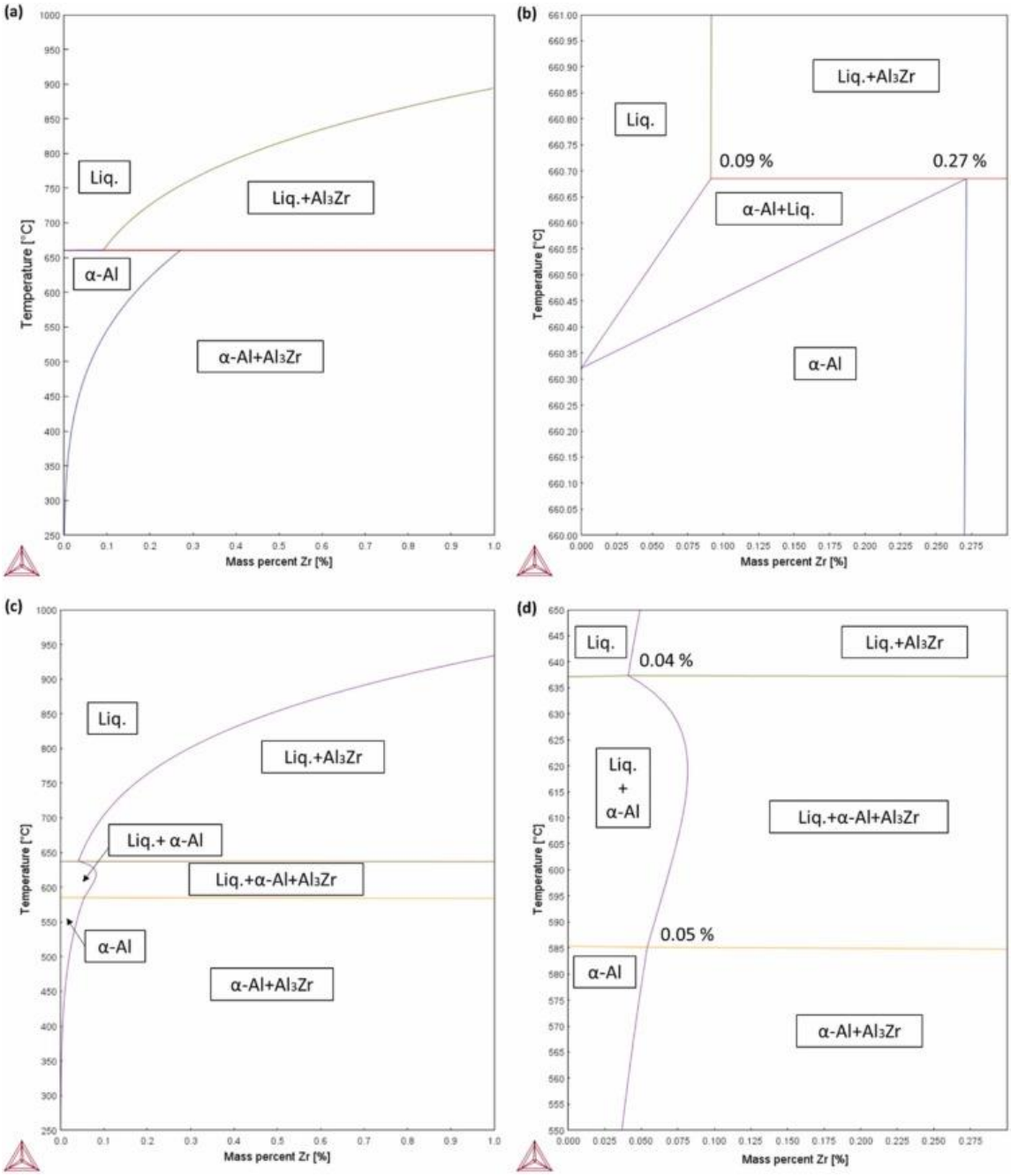

Fig. 4. Simulations of the equilibrium phase diagram of a-b) Al-Zr and c-d) Al-Mg-Zr systems with Mg= 4.5 wt%.

Simulations of the precipitation kinetics at 350 °C were performed using TC-PRISMA according to Langer-Schwartz theory [30] to investigate the synergistic effect of Zr and Sc during aging. The concentrations of Sc and Zr in α-Al decrease upon cooling, as shown in the diagram reported in Fig. 5(a), which was calculated according to the Scheil model. Given these results, it is expected a concentration gradient within cells, with higher concentration of Zr and Sc at cell cores. Those values were used to perform simulations of precipitation during aging. Fig. 5(b-c) depicts the mean radius and the volume fraction of secondary Al3(Sc,Zr) particles as a function of aging time and wt% of Sc and Zr. No formation of secondary Al3Zr

precipitates was detected by aging simulations. For times longer than 10 h, moving from the core to the boundary of cells, a decrease of the mean radius of particles is first noticeable, then the mean radius increases (while volume fraction decreases), leading to more isolated and coarser particles. These behaviors are strictly related to the supersaturation degree that is responsible for the size of critical radius for stable nuclei. Lower supersaturation degrees lead to the formation of coarser nuclei and to the dissolution of the smaller ones, promoting an earlier coarsening of precipitates. A detailed description of the model can be found in Ref. [31]. Specifically, four main stages can be identified:

1) Nucleation: the size of nuclei is constant and their number density quickly increases.

2) Growth: the number density of nuclei is constant and the precipitate size sharply increases, overcoming the critical radius. At this stage, precipitates follow a normal size distribution and they grow together.

3) Transition between growth and coarsening: the supersaturation degree decreases, leading to a larger critical radius. When the critical radius enters the particles size distribution range, the smallest precipitates become unstable and particle size distribution shape starts to evolve. During this stage, the particle size distribution becomes wider, whereas the mean radius is maintained constant.

4) Coarsening: when critical radius overcomes the mean particle radius, precipitates coarse and the precipitate number density decreases.

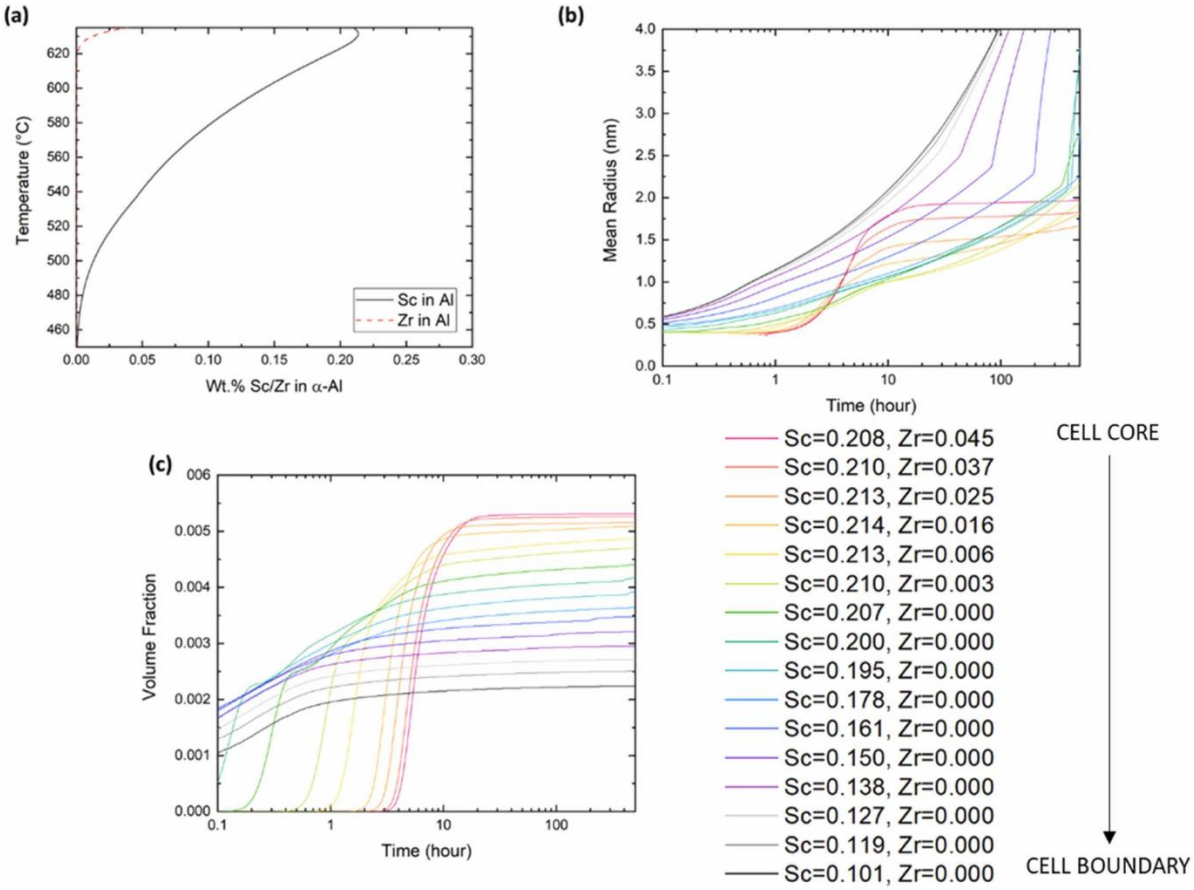

Fig. 5. a) Weight percent of Sc and Zr in α-Al during solidification. b) Mean radius and c) volume fraction of Al3(Sc,Zr) phase as a function of time and wt% of Sc and Zr, respectively.

In Fig. 2(b-c), the first three stages are noticeable for high contents of Sc and Zr. In the nucleation stage the mean radius and volume fraction is limited, whereas the growth and transition stages are visible for times longer than 1 h. At the boundary of cells, i.e. for lower supersaturation degrees, the critical radius sharply increases at the beginning of precipitation, leading to coarser and isolated nuclei. Thus, transition and coarsening stages occur earlier, promoting the formation of larger mean radii and volume fractions (Fig. 5(b) and (c), respectively).

3.2. As-built microstructure

LOM and SEM images were collected on the vertical section (parallel to the building direction) of AB specimens after chemical etching with Keller's reagent (Fig. 6). The micrograph of Fig. 6(a) shows a fish-scale pattern composed by tiny solidified melt pools having an average width of 160 μm and a depth of 50 μm. Few occasional pores and no evidence of cracks were found in the investigated cross sections. The SEM images of Fig. 6(b-c) show solidification cells and dispersed bright submicron-sized particles. EDS chemical analysis was carried out on these precipitates and results are reported in Table 2, indicating a high content of Zr and Sc. Thus, such submicron-size particles are likely L12-Al3(Sc,Zr) particles that precipitated in liquid phase and are responsible for grain refining. EDS chemical analysis on wider surfaces

performed on AB samples showed a loss of ~ 0.7 wt% Mg after the printing process due to the evaporation of Mg atoms from the melt pool during LPBF (see Tables 1 and 2 for comparison).

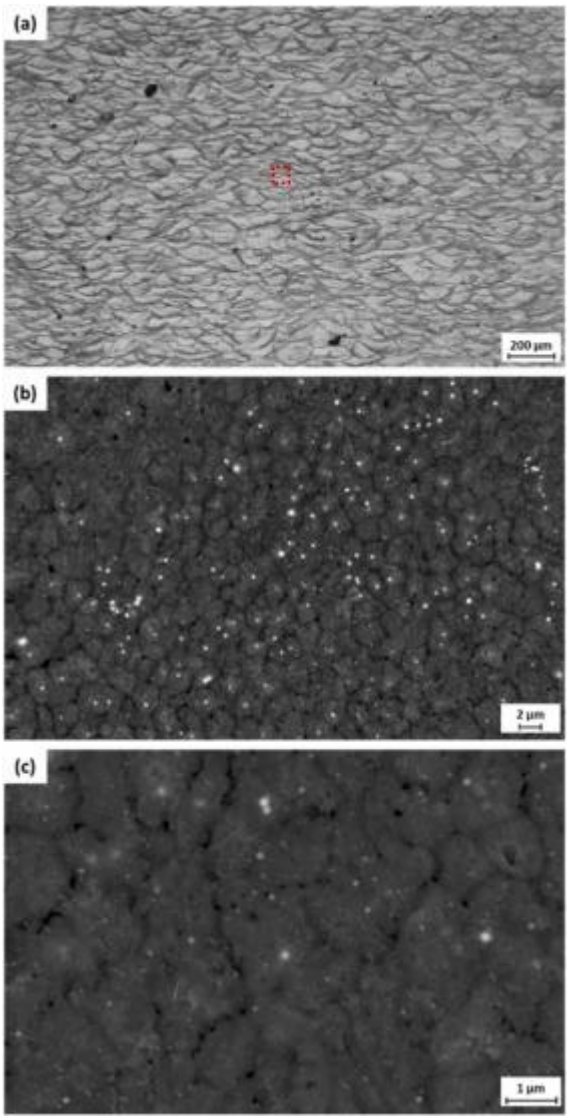

Fig. 6. a) Optical micrograph and b-c) low- and high-magnification SEM images collected on the vertical section of AB sample after chemical etching with Keller's reagent. The red square in Fig. 6(a) highlights the spot where SEM images were taken.

Table 2. EDS chemical analysis performed on bright submicron-sized particles in Fig. 6(b-c) and on AB samples. The standard deviation on EDS measurements performed on AB samples is< 0.1 wt%.

	Mg	Sc	Zr	Al
Submicron-sized particles	3.8 (±0,1)	0.6 (±0,2)	2.5 (±0,2)	Bal.
AB	4.5	0.3	0.8	Bal.

EBSD analyses were carried out on vertical sections parallel to the building direction of AB specimens. The IPF map of the α-Al phase is reported in Fig. 7 along with the IPFs and grain size distribution histograms of the two selected areas. Fine grains elongated along the building direction formed in the upper part of the melt pools, whereas submicron-sized equiaxed grains are visible above the melt pool boundaries. Accordingly, the AB microstructure features a bimodal grain size distribution, with the average grain area decreasing from 3.73 μm2 to 0.52 μm2 passing from the elongated- to the equiaxed-grain zone (Fig. 7(e) and (d), respectively)), indicating different mechanisms of solidification that occur at melt pool core and boundary. IPFs collected in the zone with elongated grains show a slight (100) and (101) texture along the transversal (X) direction and along normal and building (Z and Y) directions, respectively (Fig. 7(c)). On the contrary, the zone with a fine equiaxed microstructure reveals lower gap between minimum and maximum pole densities (Fig. 7(b)).

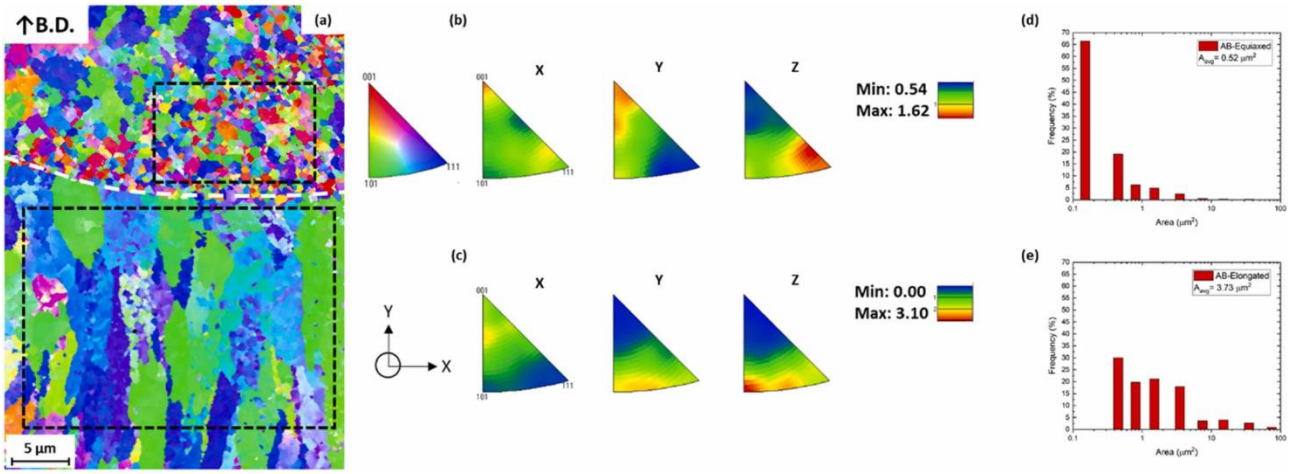

Fig. 7. a) IPF orientation map of α-Al phase, b-c) IPFs and d-e) grain size distribution collected on regions with fine equiaxed grains and elongated grains, respectively.

3.3. Aging treatment and mechanical properties

DSC scans with an heating rate of 20, 30 and 40 °C/min were performed on AB samples to evaluate the aging response of the alloy right after solidification. The curves are reported in Fig. 8. Two exothermic peaks (A and B) and one endothermic peak (C) were identified and shown in the thermogram. Specifically, the exothermic peaks A and B could be ascribed to precipitation of continuous and discontinuous Al3(Sc,Zr) particles, respectively [32], [33], whereas the endothermic peak C could be related to the dissolution of Al3Mg2 phase formed at the end of solidification [34].

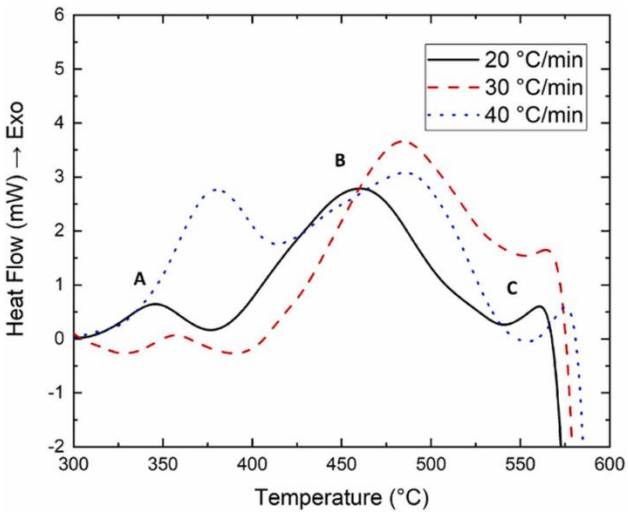

Fig. 8. DSC curves of the AB Al-Mg-Zr-Sc alloy collected with an heating rate of 20, 30 and 40 °C/min.

Aging tests at 300 °C, 350 °C, 375 °C and 400 °C were also performed to monitor the material hardness evolution as a function of time. As depicted in Fig. 9, the hardness of the AB alloy increased from 105 HV to 160 HV after 24 h of aging at 350 °C. Aging curves collected at 375 °C and 400 °C showed similar trends and a comparable peak hardness of ~155 HV after 8 h. Lower values are noticeable in the aging curve collected at 300 °C, indicating a more sluggish precipitation kinetics. Indeed, the hardness peak could be achieved for times longer than 24 h, whereas the slight hardness increase detected between 12 h and 24 h could be ascribed to coarsening of secondary Al3(Sc,Zr) particles.

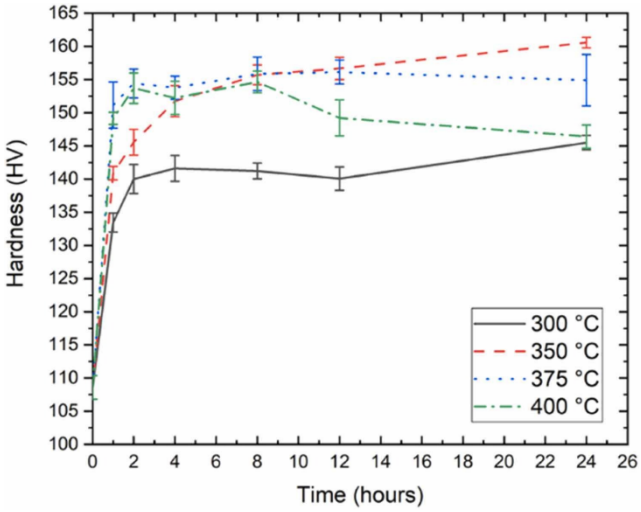

Fig. 9. Aging curves collected at 300 °C, 350 °C, 375 °C and 400 °C.

The microstructure of samples aged at 375 °C to the hardness peak was investigated by SEM (Fig. 10). Fig. 10 (a) reveals grains elongated towards the building direction adjacent to regions with a submicron-size grain structure. These zones are decorated by a large amount of bright particles with quasi-spherical shape, located both at the center of grains and along grain boundaries (Fig. 10 (b-d)). Due the relatively large size of these particles, they could be related to primary Al3(Sc,Zr) and Al3Zr precipitation. EDS analysis was performed on spots labeled as

A and B in Fig. 10 (c) and reported in Table 3. A content of Sc and Zr higher than that found in the average chemical composition of the AB alloy (Table 2) was detected.

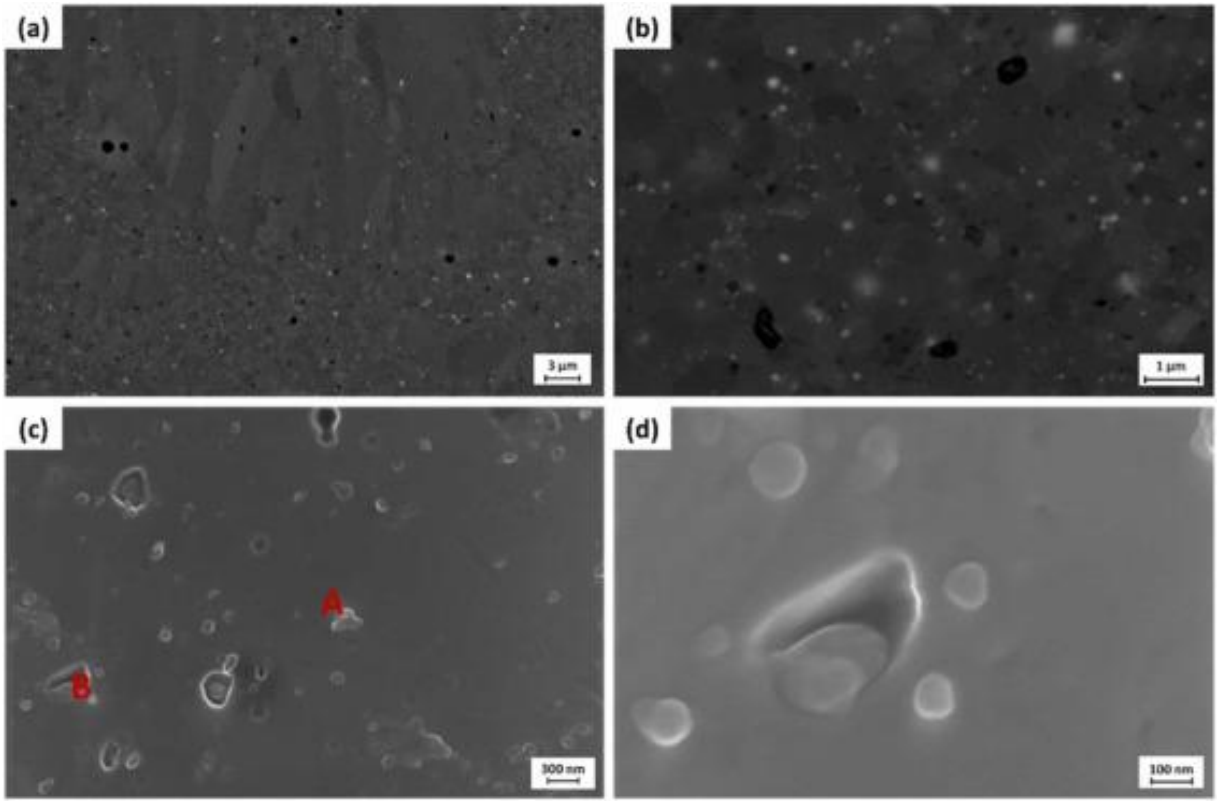

Fig. 10. a) Low-magnification BSE-SEM images collected on the vertical section of aged samples. High-magnification b) BSE- and c-d) Inlens-SEM images of the zone with submicron-size grains.

Table 3. EDS chemical analysis performed on spots labeled as A and B in Fig. 10 (c).

	Mg	Sc	Zr	Al
Spot A	4.0	0.5	2.5	Bal.
Spot B	4.1	0.6	3.0	Bal.

EBSD analyses were carried out on aged samples and orientation map of α-Al phase, IPFs and grain size distribution histogram are shown in Fig. 11. Aging does not appreciably affect the grain structure, indeed, a microstructure featuring zones with submicron-sized equiaxed and fine elongated grains was detected in both AB and aged samples.

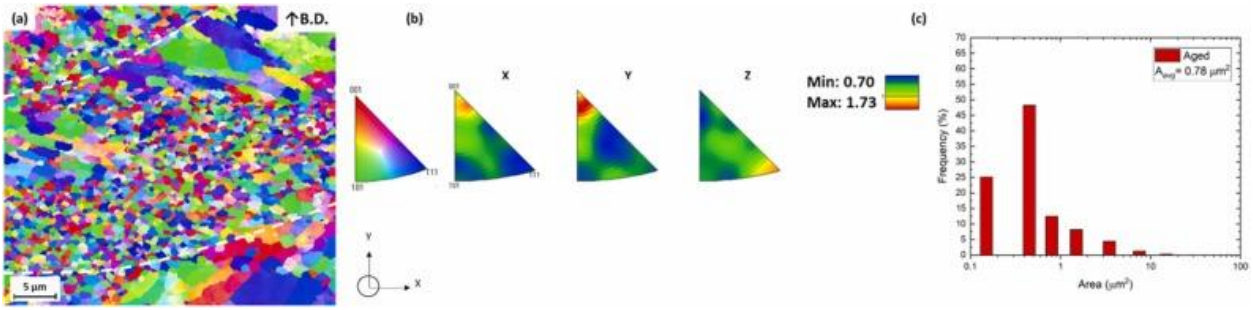

Fig. 11. a) Orientation map of α-Al phase, b) IPFs and c) grain size distribution collected on aged samples.

Crystallographic macro-texture investigations were performed by XRD equipped with Eulerian cradle. Results are reported in Fig. 12. IPFs of the AB alloy revealed a slight texture induced by grains with< 100 > and< 101 > directions oriented along [ND], [TD] and [RD] directions. As also observed by EBSD analysis, the aging treatment does not severely affect the texture. Only a slight decrease of the maximum pole density of the [TD] IPF was detected, passing from 2.75 to 1.73 after the aging treatment.

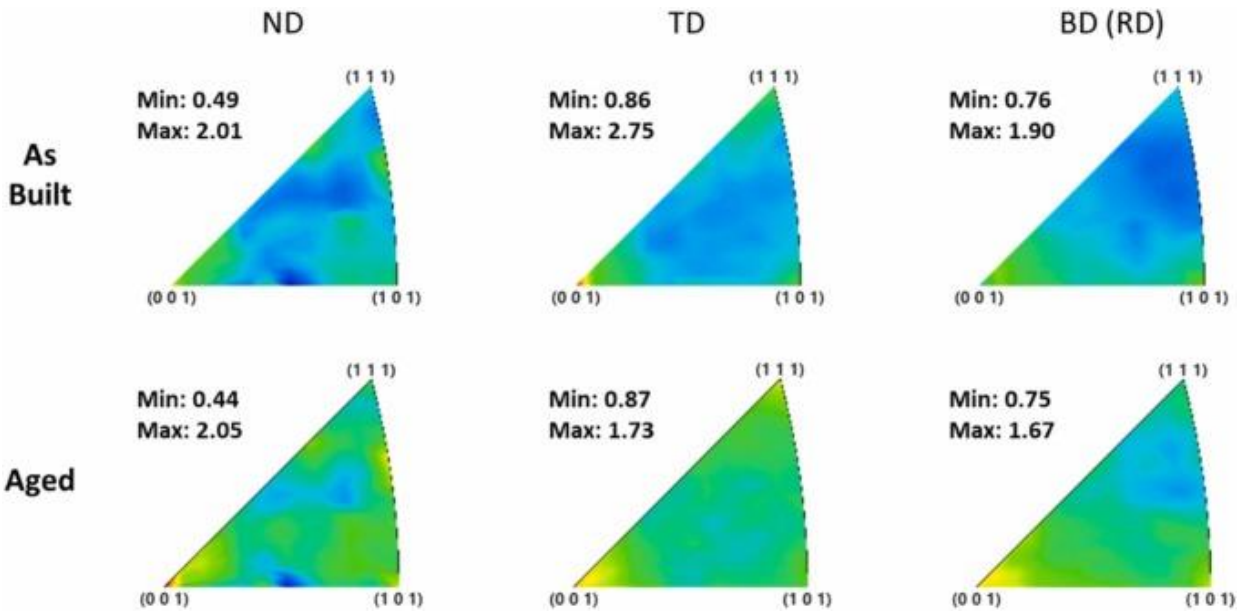

Fig. 12. IPFs collected on the vertical section of a) AB and b) aged alloy.

Residual stresses were measured on the lateral surface of AB samples and their evolution as a function of the aging time was monitored in order to investigate the stress relief ability of the annealing treatment. The aging temperature was set at 375 °C and results are reported in Fig. 13. The AB condition shows σI and σII tensile residual stresses of 90 MPa and 56 MPa, respectively. Aging leads to a slight increase of σI after 1 h (124 MPa). After 8 h of aging, i.e. the time that is needed to reach the hardness peak, σI and σII decrease to 38 MPa and − 13 MPa, respectively, then they keep quite stable.

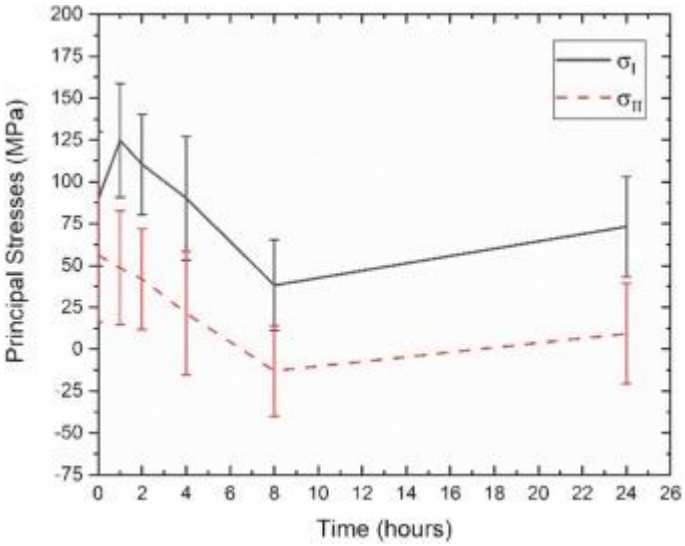

Fig. 13. Residual stress measurements as a function of aging time.

Tensile tests were performed on peak-aged specimens (i.e. treated at 375 °C and 350 °C for 8 h and 24 h, respectively) with longitudinal axis perpendicular to the building direction. Representative tensile curves are reported in Fig. 14 and mechanical properties are summarized in Table 4 and compared with those of the as-built alloy provided by the supplier [35]. The alloy in the aged condition shows similar values of strength and fracture elongation. Tensile records show an upper and lower yield strength and serrations in the plastic region.

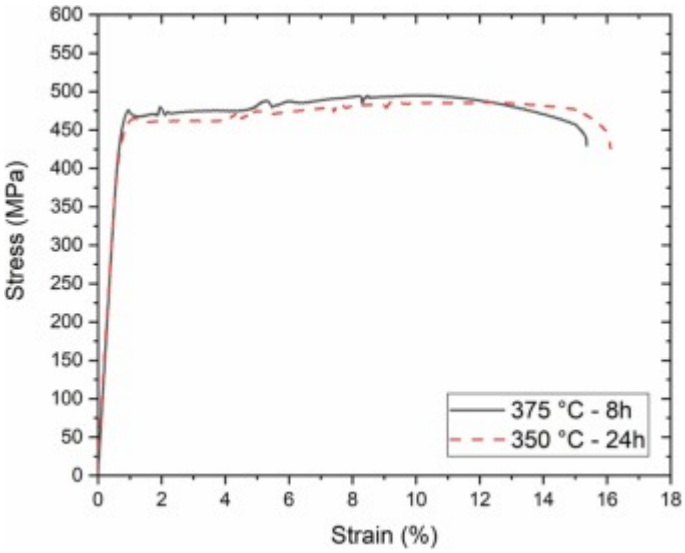

Fig. 14. Representative tensile curves of the Al-Mg-Zr-Sc alloy heat treated at 375 °C and 350 °C for 8 h and 24 h, respectively.

Table 4. Mechanical properties of the Al-Mg-Zr-Sc alloy heat treated at 375 °C and 350 °C for 8 h and 24 h, respectively.

	Yield Strength [MPa]	Tensile Strength [MPa]	Elongation at Fracture [%]
Aged 375 °C – 8 h	460 (±10)	489 (±6)	14.3 (±2.7)
Aged 350 °C – 24 h	454 (±2)	485 (±3)	12.1 (±4.0)
As-built	280	350	23

4. Discussion

In this study, an Al-5.2Mg-0.8Zr-0.3Sc alloy was successfully processed by L-PBF, showing almost full density and no cracks. Simulations of the Scheil curve of the Al-Mg-Zr-Sc alloy show that the precipitation of Al3Zr starts at 910 °C in the molten liquid. Sc intervenes in the precipitation reaction with the formation of Al3(Sc,Zr) phase at 684 °C, followed by the solidification of α-Al grains (Fig. 3(a)). SEM images and EDS analyses (Fig. 6(b-c) and Table 2) performed on AB specimens consistently show a dispersion of Zr- and Sc-rich particles preferentially located within submicron-sized α-Al grains. They are supposed to be Al3(Sc,Zr) and Al3Zr predicted by Scheil simulations acting as nucleation sites for new grains. Small grains are mainly located at melt pool boundaries, as shown by EBSD analyses (Fig. 7(a)). In such areas, the high cooling rates involved in LPBF lead to a strong undercooling leading to higher nucleation rate of α-Al grains. Moving towards the center of the melt pool, due to lower thermal gradients, recalescence effect and higher growth rates [5], [36], a competitive solidification mode occurs and grains become relatively coarser and elongated along the maximum heat flow directions, as shown in Fig. 7(a,c,e). Accordingly, (100) and slight (101) texture is found in the center of the melt pool (Figs. 7(c) and 12), whereas no crystallographic texture was detected in the zones with fine equiaxed grains (Fig. 7(b)).

Sc and Zr are also able to precipitate as Al3(Sc,Zr) particles from a super-saturated solid solution during the aging treatment [16], [37], [38]. The super-saturated solid solution is attained by the high cooling rates produced by the LPBF process, when solute atoms are trapped within the α-Al matrix and create a meta-stable extension of the solubility (super saturated solid solution, SSSS) [39]. As reported in the phase diagrams of Fig. 4, the maximum solubility limit of Zr in α-Al at equilibrium is very limited, passing from 0.27 wt% to 0.05 wt% in the Al-Zr and Al-4.5Mg-Zr system, respectively. Sc features a low solubility in α-Al as well, with a maximum of 0.11 wt% that drastically decreases with temperature [19]. The precipitation of secondary Al3(Sc,Zr) phase occurs when the AB alloy is exposed at elevated temperatures (~350 °C) and the SSSS evolves into equilibrium phases [16], [19], [24]. The exothermic peaks A and B of DSC scans reported in Fig. 8 confirmed this precipitation phenomenon. Aging performed at 350 °C is therefore supposed to favor continuous precipitates leading to an increase of micro-hardness from 105 HV to 160 HV after 24 h (Fig. 9). It is worth noting that no secondary Al3Zr phase forms during aging according to simulations (Fig. 5), indicating the

need of a synergistic effect brought by Sc in the precipitation sequence. This is in good agreement with previous studies performed on Al alloys with Sc and Zr [20], [22], [40].

SEM images and EBSD investigations performed on aged samples show microstructural features similar to those of the AB alloy (Figs. 10 and 11, respectively), as well as no strong differences were detected regarding micro- and macro-texture analyses (Figs. 11 (b) and 12, respectively). Indeed, the bimodal grain size distribution is still visible after the aging treatment, even though the treatment is performed at high temperature, probably due to pinning effect to grain boundary migration promoted by Sc\Zr-based intermetallic particles shown by the SEM/EDS analyses (Fig. 10 (b-d) and Table 3).

The evolution of residual stresses and micro-hardness values during aging at 375 °C was monitored as a function of time starting from the AB condition. Fig. 9 shows a sharp increase of the hardness value, passing from 105 HV to 150 HV after 1 h of aging, indicating a copious precipitation of strengthening particles. Simultaneously, a slight increase of tensile residual stresses is noticeable (Fig. 13), probably induced by the lattice mismatch between strengthening particles and α-Al matrix [41]. Buranova et al. performed geometric phase analysis (GPA) mapping to investigate elastic strains around Al3Sc particles and showed that the misfit between the coefficient of thermal expansion of Al3Sc and α-Al leads to residual stress fields among those precipitates [42]. At higher aging time, residual stresses decrease, with σI and σII passing from 124 MPa and 48–38 MPa to − 13 MPa after 8 h of aging, whereas the hardness peak (156 HV) was detected after 8 h. In light of these results, a direct aging performed at 375 °C and 8 h is capable to substantially relax the residual stress field and simultaneously maximize the micro-hardness of the Al-Mg-Z-Sc alloy due to precipitation of strengthening particles.

Tensile tests were performed on alloys annealed at the peak hardness condition, namely at 375 °C and 350 °C for 8 h and 24 h, respectively. The alloy showed YS and UTS values of 460 MPa and 485 MPa in both conditions (Table 4). Tensile records reveal an upper and lower yield strength and serrations in the strain-hardening field. This phenomenon is commonly found in Al-Mg alloys produced by conventional methods due to the high solubility of Mg within the α-Al matrix [43], [44]. Indeed, the stress field associated to solute atoms interact with that of mobile dislocations during deformation, leading to dynamic strain aging and subsequent serrations in the plastic flow. The high content of Mg in the Al-Mg-Zr-Sc alloy combined with the wide super-saturated solid solution promoted by the high cooling rates of LPBF is therefore responsible for serrations in Fig. 14.

The enhanced mechanical properties of the m4p™ StrengthAl alloy can be ascribed to different strengthening mechanisms. Specifically, contributions related to solid-solution, grain-boundary (Hall-Petch) and particles strengthening (anti-phase boundary and Orowan mechanisms) were computed and compared with experimental results. Equations and parameters used for calculations of strengthening contributions are reported in Appendix A [45], [46], [47].

The YS of pure Al (original strength of the lattice) is ~ 10 MPa [48], which is a small contribution to mechanical performances. Due to the high solubility of Mg in α-Al, solid-solution strengthening can be ascribed primarily to Mg atoms. 4.5 wt%Mg leads to a strength increase of Δσ= 96 MPa (Fig. 15(a)). A large contribution to the increment of YS is related to the Hall-Petch effect. Due to the bimodal grain size distribution found in samples (Fig. 10 (a)), it is difficult to accurately define an average value of grain size. Considering the zone with relatively coarser and elongated grains as the most susceptible to yielding [49], [50], a grain area of 3.73 μm3 can be taken as reference value from EBSD analysis (Fig. 7(e)), leading to a Δσ= 97 MPa (Fig. 15(b)). Finally, both primary and secondary Al3(Sc,Zr) particles contribute to strengthening by resistance to dislocation motion. Specifically, two different mechanisms must be taken into account to accurately predict the increment of YS. The anti-phase boundary (APB) model describes the cutting of particles by dislocation motion, whereas the Orowan effect considers the pile-up and bowing of dislocations at the particle-matrix interface. Nano-sized coherent particles are subjected to cutting, thus enhancing the YS of the alloy by order (Δσord) and coherency and modulus (Δσcoh+mod) strengthening mechanisms [45]. The former is due to the energy associated to the new chemical bonds that are created between the precipitate and the matrix [46]. The latter relies on the strain field arising at the particle-matrix interface due to lattice mismatch and to the different shear modulus between the precipitates and the Al matrix, respectively. Therefore, the higher value between Δσord and Δσcoh+mod has to be considered for calculation of Δσ [51]. Increasing the particles size, bowing of dislocations becomes energetically favored, so Orowan model governs the strengthening mechanism above a critical radius (rcrit). As a sake of example, Fig. 15 (c) shows the particle strengthening trends for a volume fraction (fvol) of 0.005. A particle radius ranging from 25 nm to 120 nm was computed by image analyses performed on SEM images reported in Fig. 10 (c-d). Due the relatively large size of these particles, they could be related to primary Al3(Sc,Zr) and Al3Zr precipitation. The fvol of primary particles was calculated through numerical simulations (fvol=0.0119). Assuming that the particle size is much higher than rcrit, the Orowan model has been considered, resulting in a Δσ= 80 MPa. The mean radius and fvol of secondary Al3(Sc,Zr) particles after 24 h at 350 °C (hardness peak) were computed by precipitation simulations at different cell locations (Fig. 5(b-c)). Order, coherency and modulus and Orowan strengthening contributions were calculated for each radius and fvol. Coherency and modulus strengthening dominates the strengthening mechanism and an evolution of Δσcoh+mod was evaluated for different cell positions, from cell core to cell boundary, i.e. as a function of the solidified α-Al (Fig. 15 (d)). The data were fitted using a 2nd order polynominal curve, that was integrated to calculate the overall increment in strength due to secondary precipitation (Δσ=167 MPa). By adding up all the Δσ contributions (Table 5), a final YS of 450 MPa is achieved, which is in good agreement with experimental results obtained for the aged alloy (Table 4), indicating that the major strengthening mechanisms in the m4p™ StrengthAl alloy processed by LPBF are related to secondary particles strengthening. Furthermore, a YS of 280 MPa was reported by the supplier for the as-built alloy, in agreement with the sum of lattice, solute, grain boundary and primary precipitation contributions (283 MPa).

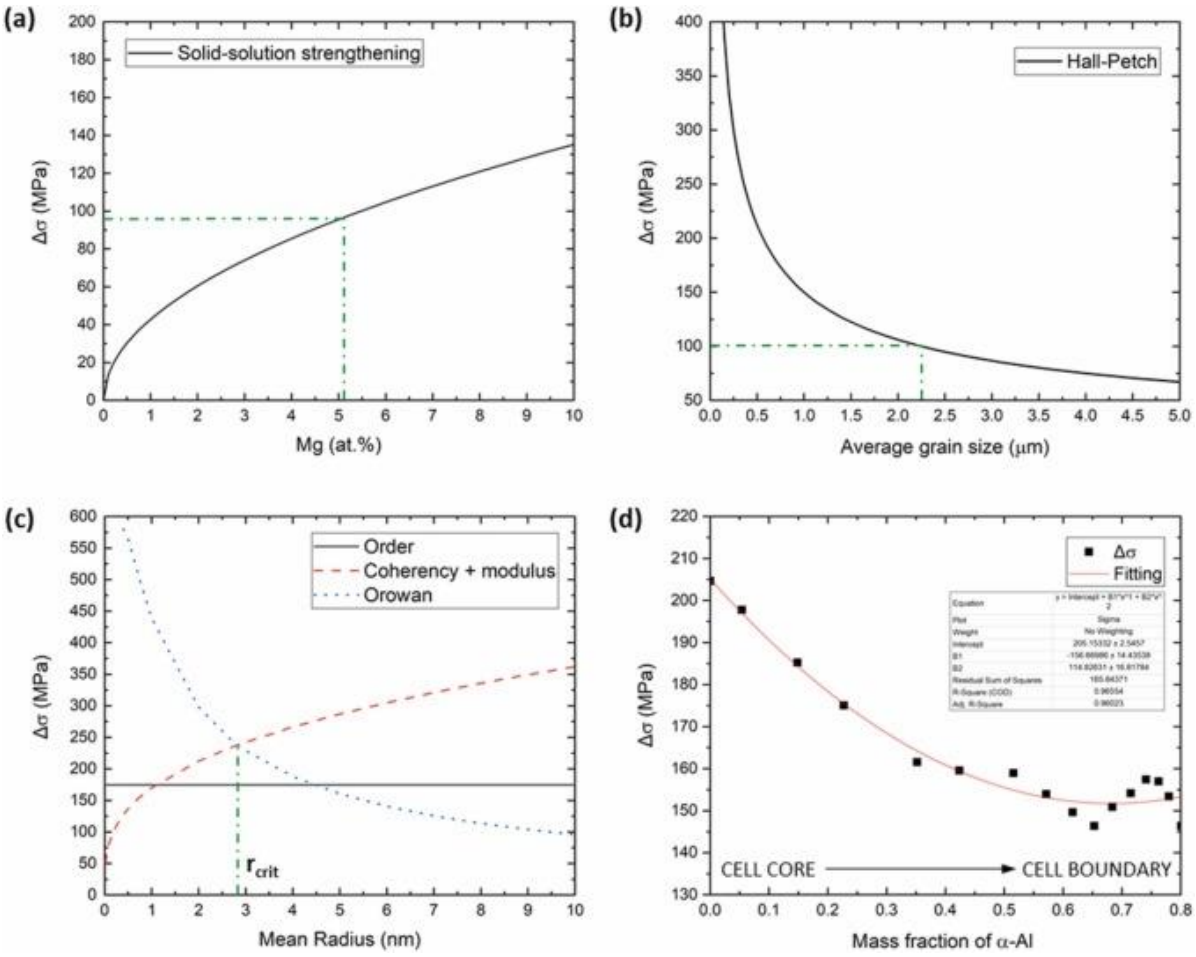

Fig. 15. Theoretical increase in YS related to a) solid-solution, b) grain refinement and c) particles strengthening for fvol= 0.005. d) Evolution of secondary particles strengthening as a function of the mass fraction of solidifying α-Al (computed by ThermoCalc simulations).

Table 5. Contributions to YS computed using strengthening models.

Lattice	Solute	Grain boundary	Primary precipitation	Secondary precipitation
10	96	97	80 (Orowan)	167 (Coherency + modulus)

Finally, an histogram is reported in Fig. 16 to resume the mechanical performances of aged Al-Mg-Zr-Sc alloy investigated in this work and compare them with those of other commercial Al alloys processed by LPBF. The m4p™ StrengthAl alloy shows higher YS, UTS and Ɛr than conventional Al-Si systems and a slightly higher YS than A20X™ [12]. On the contrary, Scalmalloy® exhibits moderately better mechanical properties (YS=480 MPa, UTS= 520 MPa and Ɛr =13% [52]) than the investigated alloy, likely due to the higher content of Sc.

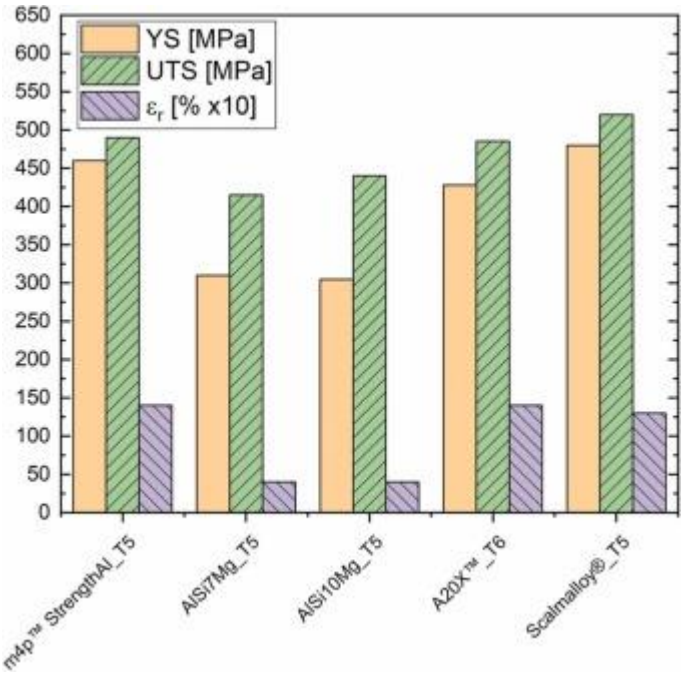

Fig. 16. Mechanical properties of AlSi7Mg, AlSi10Mg, A20X™, Scalmalloy® and m4p™ StrengthAl alloy investigated in this study [12], [52].

5. Conclusions

An Al-Mg-Zr-Sc alloy with reduced content of Sc, commercially available as m4p™ StrengthAl, was successfully processed by Laser Powder Bed Fusion. The main conclusions can be summarized as follows:

• Zr-based submicron-sized particles were found within α-Al grains and along grain boundaries in the as built material.

• Fine equiaxed grains at melt pool boundaries and elongated grains at melt pool cores were noticeable both in the as built and heat treated alloy.

• The annealing treatment does not have a strong influence on both grain size and crystallographic texture of the alloy.

• The formation of secondary Al3(Sc,Zr) particles during the annealing treatment led to a sharp increase of material micro-hardness and tensile properties and a reduction of residual stresses.

• YS and UTS values of 460 MPa and 485 MPa were recorded in samples aged at 350 °C and 375 °C for 24 h and 8 h, respectively.

• The strengthening mechanisms leading to the above properties have been evaluated on a theoretical basis. It has been shown that the major strengthening mechanism is related to strengthening by precipitation of secondary Al3(Sc,Zr) particles during aging.

Despite the reduced amount of Sc compared to other commercial Al alloys, the mechanical performance of the investigated alloy revealed to be remarkable. The use of a well balanced

combination of Sc and Zr is considered as an interesting feature of the investigated alloy, which is more compliant with the guidelines of EU on the use of critical raw materials.

CRediT authorship contribution statement

F. Belelli: Conceptualization, Methodology, Validation, Formal analysis, Writing – original draft, Investigation. R. Casati: Conceptualization, Methodology, Writing – review & editing, Supervision, Project administration, Funding acquisition. C. Andrianopoli: Resources, Writing – review & editing. F. Cuccaro: Validation, Formal analysis, Investigation. M. Vedani: Conceptualization, Writing – review & editing, Supervision, Project administration, Funding acquisition.

Declaration of Competing Interest

The authors declare the following financial interests/personal relationships which may be considered as potential competing interests: C. Andrianopoli reports a relationship with m4p material solutions that includes: employment.

Acknowledgments

The present research was partially funded by the EIT Raw Materials project SAMOA (Sustainable Aluminum Additive Manufacturing for high-performance applications, no. 18079). The Italian Ministry of Education, University and Research is acknowledged for the support provided through the Project "Department of Excellence LIS4.0 - Lightweight and Smart Structures for Industry 4.0.

Appendix A

The increment in YS for solid solution strengthening is computed as:

$$\Delta\sigma = \frac{3.1\varepsilon G c^{1/2}}{700} \quad (1A)$$

where σy, ε, G and c are the yield strength, an experimental constant equals to 3.8 * 10−7, the shear modulus of Al (25.4 GPa) and the atomic percentage of Mg atoms in solid-solution, respectively [48].

The Hall-Petch equation is reported in the following:

$$\sigma_y \propto \frac{k}{\sqrt{d}} \quad (2A)$$

in which d is the average grain size and k is a parameter taken equals to 0.15 MN/m3/2 for Al-Mg alloys [53]. The YS increments for order strengthening, coherency and modulus strengthening and Orowan strengthening were computed as follows [45], [46], [47]:

$$\Delta\sigma_{ord} = 0.81M\frac{\gamma_{APB}}{2b}\left(\frac{3\pi f_{vol}}{8}\right)^{1/2} \quad (3A)$$

where M= 3.06 is the mean matrix orientation factor, b = 0.286 is the magnitude of the Burgers vector in Al, fvol is the volume fraction of strengthening particles and γAPB = 0.5 J/m2 is the anti-phase boundary energy of precipitates;

$$\Delta\sigma_{coh} = 2.6M(G\varepsilon)^{3/2}\left(\frac{<r>f_{vol}}{0.5\,Gb}\right)^{1/2} \quad (4A)$$

where ε = 0.88% is the lattice parameter mismatch and<r > is the mean particle radius;

$$\Delta\sigma_{mod} = 0.0055M(\Delta G)^{3/2}\left(\frac{2f_{vol}}{Gb^2}\right)^{1/2} b\left(\frac{<r>}{b}\right)^{0.275} \quad (5A)$$

where ΔG= 42.5 GPa is the shear modulus mismatch between the matrix and the precipitates;

$$\Delta\sigma_{Or} = M\frac{0.4}{\pi}\frac{Gb}{\sqrt{1-\nu}}\frac{\ln\left(\frac{2<r>}{b}\right)}{\lambda} \quad (6A)$$

where v = 0.34 is the Poisson's ratio of the matrix and λ is the inter-precipitate distance, computed as:

$$\lambda = \left[\left(\frac{3\pi}{4f_{vol}}\right)^{\frac{1}{2}} - 1.64\right] < r > \quad (7A)$$